Article:

Kana Padinharu, D.K., Li, G.-J. orcid.org/0000-0002-5956-4033, Zhang, G.-B. et al. (4 more authors) (2025) Direct-drive Vernier machine with innovative stator design for enhanced demagnetization withstand capability. IET Electric Power Applications, 19 (1). e70032. ISSN 1751-8660

https://doi.org/10.1049/elp2.70032

IET Electric Power Applications

WILEY

The Institution of Engineering and Technology

ORIGINAL RESEARCH OPEN ACCESS

Direct-Drive Vernier Machine With Innovative Stator Design for Enhanced Demagnetisation Withstand Capability

Dileep Kumar Kana Padinharu[1] | Guang-Jin Li[1] | Guang-Bo Zhang[1] | Zi-Qiang Zhu[1] | Peng Wang[1] | Richard Clark[2] | Ziad Azar[2]

[1]Department of Electronic and Electrical Engineering, The University of Sheffield, Sheffield, UK | [2]Siemens Gamesa Renewable Energy Limited, Sheffield, UK

Correspondence: Guang-Jin Li (g.li@sheffield.ac.uk)

Received: 9 November 2024 | **Revised:** 2 April 2025 | **Accepted:** 4 April 2025

Handling Editor: Yacine Amara

Funding: This work is supported by the UK EPSRC Prosperity Partnership 'A New Partnership in Offshore Wind' under Grant No. EP/R004900/1.

Keywords: permanent magnet generators | permanent magnet machines | wind power

ABSTRACT

This paper proposes a Vernier machine with an improved stator design that adopts open stator slots and permanent magnets installed on both the rotor and stator. Compared to an existing Vernier machine in the literature, referred to as Design 1, the exclusive stator slots for permanent magnets in the proposed machine help mitigate demagnetisation issues by physically isolating the windings and the magnets. Additionally, the open stator slot design facilitates the installation of form-wound coils which is desirable for large generators used in direct-drive wind power applications. Using 2-dimensional finite element analysis, the proposed design is compared with a conventional surface-mounted permanent magnet machine, a conventional Vernier machine and Design 1. The findings indicate that the proposed Vernier machine uses both odd and even harmonics to generate torque, and it can exhibit superior electromagnetic performance, including torque and efficiency, compared to the conventional surface-mounted permanent magnet machine and conventional Vernier machines and demonstrate comparable electromagnetic performance to Design 1. Furthermore, to enhance the torque-to-mass ratio of the proposed Vernier machine, through-slots below the stator magnets are introduced and found to be effective without significantly compromising torque and efficiency. The simulations have been validated by experiments based on a prototype.

1 | Introduction

Direct-drive permanent magnet (PM) machines are increasingly popular for wind power applications particularly for offshore installations [2]. This is mainly due to the frequent maintenance and failures associated with gearboxes, which are used to increase generator speed but reduce their torque, thereby lowering generator sizes and costs. Direct-drive technology eliminates the gearbox by directly coupling the turbine shaft to the generator, making the drive train system simpler and more efficient. However, because of their lower generator speed, the direct-drive machines must produce much higher torque than their geared counterparts to achieve the same output power. This results in bulkier and more costly generators. Consequently, extensive research is underway to improve the torque density of wind generators.

Recently, Vernier machines have become popular because of their high torque density and simple structure as shown in Figure 1b. Moreover, their multi-pole structure and inherent

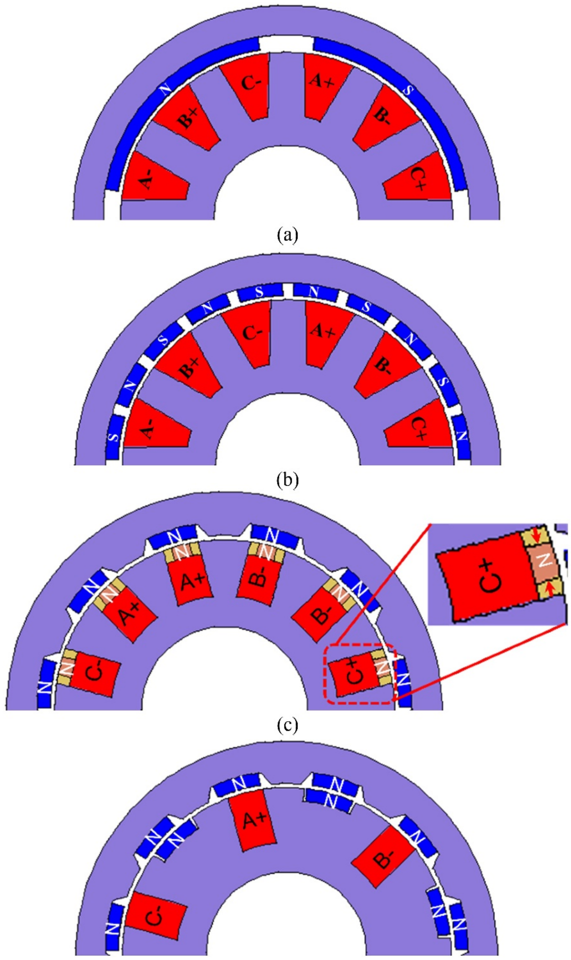

FIGURE 1 | Comparison of 2D models between (a) conventional SPM, (b) conventional SPM-V, (c) Design 1 [1] and (d) proposed Vernier machine.

low torque ripple make them well-suited for low speed direct-drive applications [3–5]. They use the flux modulation/magnetic gear principle to generate high torque [6]. However, compared to the conventional surface-mounted permanent magnet (SPM) machines (see Figure 1a), Vernier machines have a lower power factor [7]. To address this issue, several novel topologies were proposed in the literature to improve both the power factor and torque density of the Vernier machines [8–18].

The low inter-pole leakage flux in the Halbach PM array and the flux concentration feature of the spoke PM array were utilised to achieve high torque density compared to a classical surface-mounted PM Vernier (SPM-V) machine [8–10]. In addition, a consequent pole PM arrangement in the rotor can reduce PM usage for the same output power [11, 12, 19, 20]. To further improve torque density, topologies with either dual stators [13] or rotors [14] are also proposed. However, a dual airgap increases the complexity of the structure and is not desirable for large size multi-MW direct-drive machines. For smaller power machines, a split-teeth stator with fractional slot concentrated windings (FSCW) is proposed to improve the torque per unit volume by reducing the end-winding length [8, 15, 16].

The split-teeth stator has empty slots between the flux modulating teeth (FMT) that are typically unutilised. It has been found that by installing PMs in these empty slots, the torque of the machine could be improved significantly, leading to the development of magnets on both sides (stator and rotor) PM Vernier (MB-PMV) topologies. This topology requires rotor saliency to modulate the stator PM flux and induce voltage in the stator windings, thus generally employing consequent pole rotors. Various combinations of PM arrangements in the rotor and stator have been explored to create new topologies [21–24]. However, compared to an integer slot Vernier machine, a split-teeth stator with FSCW has to compromise torque for the advantage of shorter end windings [25]. MB-PMV topologies with open stator slots and integer slot windings are rarely found in the literature because of the difficulty of installing the PMs without empty FMT slots.

The existing open stator slot MB-PMV topology uses Halbach array PMs in the stator slot opening as shown in Figure 1c [1]. This Vernier machine could achieve 54% higher torque density with 37% larger PM volume compared to a classical SPM-V machine. However, placing the PMs in the stator slot opening close to copper windings can result in thermal issues, especially for high power/electrical loading applications. The high temperature of the windings increases the risk of PM irreversible demagnetisation which is critical for machine reliability and a key issue in Vernier machines at high power ratings. Moreover, Halbach array PMs increase the cost of the machine because of the complexity of magnetisation and installation.

To harness the advantages such as high torque density and address the aforementioned challenges such as complexity of magnet magnetisation and installation of the existing Vernier machines (see Figure 1c), this paper proposes a Vernier machine with an improved stator design as shown in Figure 1d. The stator adopts an open slot structure with single-layer integer slot windings which is ideal for high power direct-drive machines [26]. Additionally, it incorporates an exclusive stator slot, akin to the split-teeth stator, for installing the PMs. The dimension of these exclusive stator slots (opening angle and depth) are determined by the stator PMs, and they are not linked with the rotor slots. By segregating the slots for copper windings and PMs, physical isolation is achieved, easing the installation of the PMs. Moreover, the open stator slot with single-layer windings facilitates the use of form-wound coils which can be pre-wound and easily inserted into the slots. A simple PM arrangement with parallel magnetisation is employed in both the rotor and the stator, ensuring ease of installation.

To fully reveal the potential of the proposed Vernier machine, its electromagnetic (EM) performance, such as torque, power factor, efficiency, torque to mass and torque to cost as well as demagnetisation withstand capability, was compared against the conventional SPM, SPM-V machine and Design 1 [1]. Key specifications and major performance indicators, including active power, torque and power factor of the four investigated machines, will be compared thoroughly. Additionally, the proposed Vernier machine features through-slots below the stator PMs to reduce the overall mass of the machine with the potential use of these through-slots as ventilation ducts also briefly discussed in this paper.

2 | Working Principle of the Proposed Vernier Machine

The fundamental working principle of a Vernier machine with PMs installed only in the rotor is widely discussed in the literature [27]. The fundamental armature magneto-motive force (MMF) is modulated using the airgap permeance created by the open stator slots. The modulated field is then coupled to the fundamental MMF created by the rotor PMs. By harmonically coupling the armature and PM fields, the tangential component of the airgap flux density can be significantly enhanced. This enhancement helps Vernier machines generate high torque. To enable the harmonic coupling, the slot/pole number combination in a Vernier machine follows the rule given by the following equation:

$$P_r = Z - P_s \text{ or } P_r = Z + P_s \tag{1}$$

where Z is the number of stator slots, P_r is the number of rotor pole pairs and P_s is the number of stator winding pole pairs. The slot/pole number combination with $P_r = Z - P_s$ is proven to generate higher torque than $P_r = Z + P_s$ [28]. Hence, to maximise the torque capability, the present paper has also chosen the slot pole number given by the following equation:

$$P_r = Z - P_s \tag{2}$$

The proposed Vernier machine has a consequent pole structure in both the rotor and stator. Moreover, the PMs and the stator windings share half of the total number of stator slots. Therefore, the MMF generated by the stator windings and PM excitation needs to be re-analysed to gain insight into the working principle.

2.1 | Airgap Flux Density Because of Armature MMF

For the proposed Vernier machine, only half of the number of stator slots are used for stator windings. Therefore, for 3-phase machines investigated in this paper, the slots/pole/phase (q) is given by the following equation:

$$q = Z/(12P_s) \tag{3}$$

It is worth noting that Z includes both the stator winding and PM slots. Substituting Equation (3) in Equation (2), we get the following equation:

$$G_r = 12q - 1 \tag{4}$$

where G_r is the gear ratio of the Vernier machine defined as the ratio of P_r to P_s. This implies that the minimum G_r possible for the proposed Vernier machine to realise an integer slot winding, that is $q = 1$, is 11.

The armature MMF (F_c) for an integer slot winding is given by the authors in Ref. [6]

$$F_c(\theta_s, t) = \frac{3\sqrt{2}T_{ph}I_{ph}}{P_s\pi}\left[\sum_{n=1,7,13,\ldots}\frac{k_{wn}}{n}\cos(nP_s\theta_s - \omega t) + \sum_{n=5,11,17,\ldots}\frac{k_{wn}}{n}\cos(nP_s\theta_s + \omega t)\right] \tag{5}$$

where T_{ph} is series turns per phase, I_{ph} is the root mean square (RMS) value of phase current, k_{wn} is the nth harmonic winding factor, θ_s is the angular position in the airgap with respect to stator reference and ω is the electrical angular frequency.

Because of Equation (2), only the slot harmonics of the order of $\left(\frac{Z}{P_s} - 1 = G_r\right)$ can be utilised for torque production. Considering only the fundamental and the lowest order (G_r) slot harmonics, Equation (5) can be further simplified as follows:

$$F_c(\theta_s, t) = \frac{3\sqrt{2}T_{ph}I_{ph}}{P_s\pi}\left[k_{w1}\cos(P_s\theta_s - \omega t) + \left(\frac{k_{wG_r}}{G_r}\right)\cos(P_r\theta_s + \omega t)\right] \tag{6}$$

Similarly, considering only the DC and the fundamental components, the airgap permeance (Λ) of the doubly salient structure of the proposed Vernier machine is given by the following equation:

$$\Lambda(\theta_s) = \frac{g}{\mu_0}[\Lambda_{0s} + \Lambda_{1s}\cos(Z\theta_s)] \times [\Lambda_{0r} + \Lambda_{1r}\cos(P_r\theta_s + \omega t)] \tag{7}$$

where Λ_{0s} and Λ_{0r} are the DC component of the airgap permeance created independently when the rotor and stator are slotless, respectively, and their peak fundamental components are Λ_{1s} and Λ_{1r}, respectively.

The airgap flux density B_{ga}, considering only the working harmonics, is given by the following equation:

$$B_{ga}(\theta_s, t) = B_1\cos(P_r\theta_s + \omega t) + B_2\cos(Z\theta_s) + B_3\cos(P_r\theta_s + \omega t) \tag{8}$$

The three terms in Equation (8) are the result of the interaction of the armature MMF and airgap permeance terms as shown in Table 1.

2.2 | Even Order Harmonics in PM MMF

A conventional SPM-V machine has PMs of opposite polarity forming one rotor pole pair. Therefore, the MMF has symmetrical positive and negative half cycles without even order harmonics. The rotor PM MMF, the direction of which is opposite to the fundamental armature MMF, therefore, can be represented as follows:

$$F_{rPM} = \sum_{i=1,3,5\ldots} F_{ir}\cos i(P_r\theta_s + \omega t) \tag{9}$$

TABLE 1 | Airgap flux densities because of armature MMF.

Armature MMF terms	Permeance terms	Resultant airgap flux density terms
$F_1 \cos(P_s\theta_s - \omega t)$	$\Lambda_{0r}\Lambda_{1s}\cos(Z\theta_s)$	$B_1 \cos(P_r\theta_s + \omega t)$
$F_1 \cos(P_s\theta_s - \omega t)$	$\Lambda_{0s}\Lambda_{1r}\cos(P_r\theta_s + \omega t)$	$B_2 \cos(Z\theta_s)$
$F_{G_r} \cos(P_r\theta_s + \omega t)$	$\Lambda_{0r}\Lambda_{0s}$	$B_3 \cos(P_r\theta_s + \omega t)$

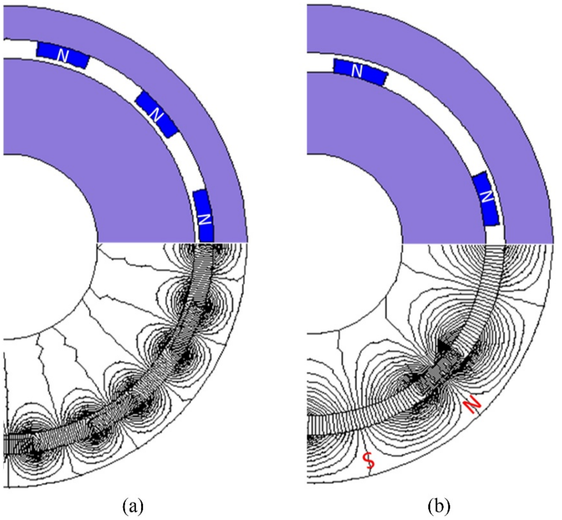

FIGURE 2 | Comparison of PM flux distribution with no slotting effect in the proposed Vernier topology. (a) Rotor PMs and (b) stator PMs.

However, for the proposed Vernier machine both the rotor and stator have consequent pole structures. The rotor/stator core acts as the virtual magnet poles with opposite polarity for the PM flux. As a result, the positive and negative half cycles of the MMF will not be symmetrical, meaning that even-order harmonics exist. To demonstrate this phenomenon, the 12-slot/11-rotor pole pair model shown in Figure 1d is analysed without considering the slotting effect. The flux distribution generated by the rotor and stator PMs is separately shown in Figure 2a,b, respectively. For a slotless model, the airgap flux density harmonic spectra represent the harmonics of the PM MMF. The comparison of radial airgap flux density spectra is shown in Figure 3. Their magnitude is normalised using their respective fundamental harmonic as reference. It can be observed that, as expected, the even-order harmonics exist in the airgap flux density generated by both the rotor and stator PMs. However, with more space between adjacent stator PMs, their even-order harmonic is significantly higher. This can be visualised in the flux distribution plot (see Figure 2b) with a low flux concentration at the centre of iron pole (virtual South pole) and a high flux concentration in stator PMs (virtual North pole).

With a negligible magnitude of even-order harmonics, the rotor PM MMF (F_{rPM}) can be approximated as Equation (9). However, the MMF created by the stator PMs (F_{sPM}), after consideration of the even-order harmonics, is given by the following equation:

$$F_{sPM} = \sum_{i=1,2,3\ldots} F_{is} \cos[i(Z/2)\theta_s] \tag{10}$$

For steady torque production, the fundamental rotor PM MMF $[F_{1r}\cos(P_r\theta_s + \omega t)]$ and the second-order harmonic of the stator

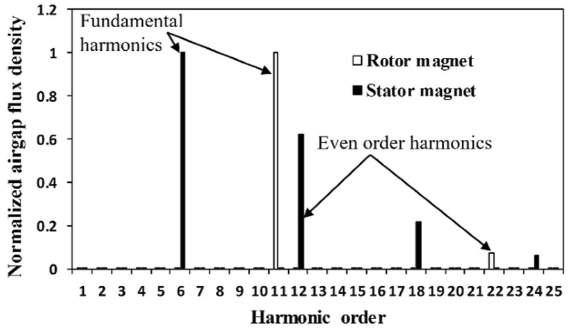

FIGURE 3 | Comparison of normalised radial airgap flux density spectra analysed in the slotless model of the proposed Vernier machine with rotor and stator PMs excited separately.

PM MMF $[F_{2s}\cos(Z\theta_s)]$ interact with the airgap flux density harmonics generated by the armature MMF as listed in Table 1. It is interesting to note that the armature MMF created a stationary airgap field $[B_2\cos(Z\theta_s)]$ which can interact with the stationary stator PM MMF for torque production. For Design 1 (see Figure 1c), instead of the even-order harmonics, the fundamental stator PM MMF $[F_{1s}\cos(Z\theta_s)]$ contributes to torque production.

3 | 2D FEA Modelling and Performance Comparison

A conventional 3 kW SPM machine was chosen to benchmark the investigated Vernier machines, that is, the conventional SPM-V, Design 1 [1] and the proposed machines. The key machine parameters are listed in Table 2. An outer rotor topology is selected as it can be directly coupled to the turbine hub and is desirable for multi-pole structures often adopted in wind generators. OPERA 2D (Dassault System), an FEA software package, was used for the analysis and optimisation of these topologies. This optimisation tool uses a combination of deterministic (sequential quadratic programming) and stochastic methods (genetic algorithms and simulated annealing). Both the conventional SPM and Vernier machines are globally optimised for maximum torque where the d-axis current is zero. The variables used for the global optimisation are the same as those discussed in [7]. These variables include the split ratio (stator outer diameter over rotor outer diameter), the magnet thickness ratio, the magnet pole arc ratio, the slot opening ratio and the stator back iron thickness ratio. For a fair comparison between the topologies, during the optimisation process, the machine volume, the copper loss, the phase current and PM volume are kept constant. It is worth noting that, the final optimised SPM-V machine has a smaller PM volume than the other machines as shown in Table 2. Because of their higher PM inter-pole leakage flux, increasing PM volume cannot further increase the torque.

TABLE 2 | Key parameters of investigated machines.

Parameters	Conventional SPM	Vernier machines		
		SPM-V	Design 1 [1]	Proposed
No. of rotor pole pair	16	66		
No. of stator slots	96	72	72	36
No. of stator winding pole pairs	16	6		
No. of stator PM pole pairs	0	0	72	36
Rated speed (rpm)	170			
Frequency (Hz)	45.3	187		
Rotor outer diameter (mm)	426.4			
Airgap length (mm)	2			
Stack length (mm)	110			
PM volume (dm^3)	0.408	0.345	0.41	0.41
Rotor PM over total PM volume ratio (%)	100	100	40	55
PM material	NdFeB ($B_r = 1.3T, \mu_r = 1.06$)			
Phase rms current (A)	2.5			
Turns/phase	832			
Phase rms voltage (V)	693	1506	1841	2140
Active power (kW)	3	4.5	5.9	6.3
Average torque (Nm)	171	254	331	354
Torque ripple (%)	24	0.38	0.63	3.4
Cogging torque (%)	13.6	0.36	0.5	2.1
Power factor	1	0.69	0.74	0.68

Hence, the machine utilises the armature reaction flux for maximising the torque by reducing the PM thickness (magnetic airgap length). A G_r of 11 has been selected for the Vernier machines as that is the minimum value possible for the proposed machine with an integer slot winding. This would result in a winding with $q = 1$ for the conventional and proposed Vernier machine and $q = 2$ for other machines. Different slot/pole number combinations are possible with this G_r. However, as an example, only the slot/pole number combination ($Z = 72, P_r = 66$ and $P_s = 6$) with optimal performance was presented in this paper (except for conventional machine). It is worth noting that a higher gear ratio is possible, however, it would worsen the power factor of Vernier machines and hence a higher gear ratio was not investigated.

3.1 | Open Circuit Flux Distribution

The comparison of one pole pair model of the investigated machines with their open circuit flux distributions (at an instant when phase A has the maximum flux linkage) is shown in Figure 4 (2 pole pairs for the conventional machine). The radial airgap flux density spectra for this flux distribution are compared in Figure 5. The slot/pole number combination for one pole pair model of the Vernier machine is $Z = 12, P_r = 11$ and $P_s = 1$. From the spectra, it can be observed that Design 1 has a 12th order fundamental created by the stator PMs in addition to the 11th order fundamental produced by the rotor PMs. Whereas, in the proposed Vernier machine with PMs installed only in half of the number of stator slots, the fundamental is the 6th order. However, as discussed before, a 12th order even harmonic is generated because of the larger space between the PMs. As mentioned previously, these 11th and 12th order harmonics can interact with the armature MMF harmonics shown in Table 1 to produce torque.

3.2 | Induced EMF and Torque

The comparison of line-line induced electromotive force (EMF) waveform and their spectra between the conventional SPM and Vernier machines is shown in Figure 6. It can be observed that the proposed Vernier machine achieves the highest induced EMF (2104 V). This is 5%, 42% and 212% higher than that generated by the Design 1, the SPM-V and the conventional SPM machines, respectively. Compared to the conventional SPM machines, the Vernier machines can achieve more sinusoidal EMFs which is beneficial for reducing the torque ripple.

The comparison of cogging torque waveforms and their spectra is shown in Figure 7. The calculated cogging torque ripples [$(CT_{max} - CT_{min})/T_{av} \times 100\%$, where CT_{max} and CT_{min} are the maximum and minimum values of cogging torque and T_{av} is the rated average torque during one electrical period] is shown in Table 2. Although the cogging torque of the proposed machine is significantly low compared to the conventional SPM machine, it is slightly higher than that of the SPM-V machine and the Design 1. It is worth noting that cogging torque reduction techniques such as skewing or PM shaping were not applied in this analysis.

Since the phase current is the same for the investigated machines, without heavy saturation, the average on-load torque will largely follow the trend of the phase EMF. The comparison of the torque waveforms is shown in Figure 8. The average

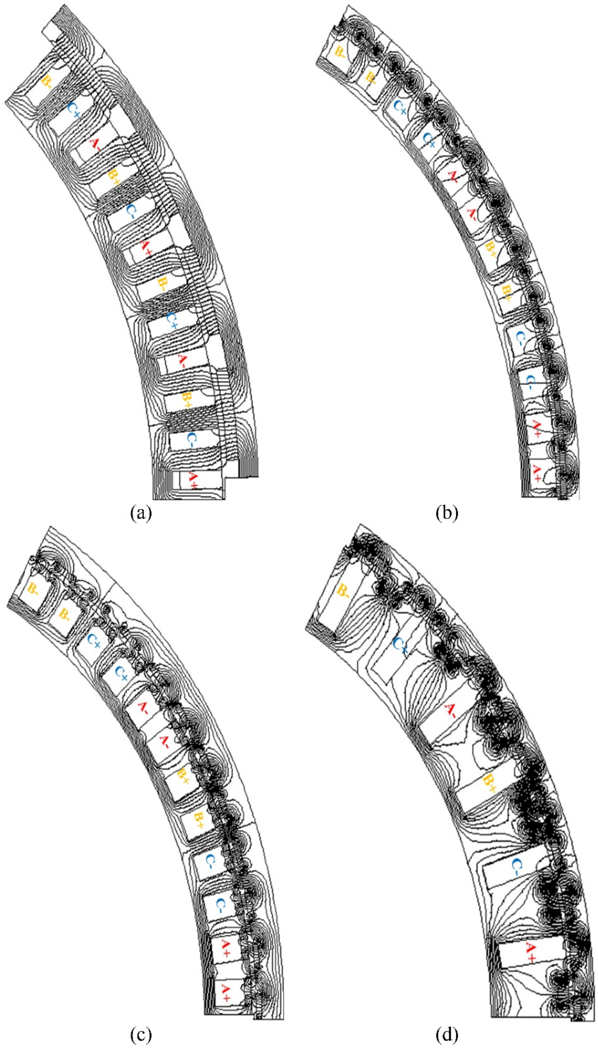

FIGURE 4 | Open circuit flux line distributions with the phase A having the maximum flux linkage. (a) Conventional SPM machine, (b) SPM-V machine, (c) Design 1 and (d) proposed Vernier machine.

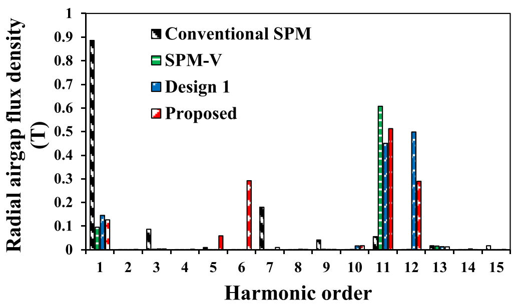

FIGURE 5 | Comparison of open circuit radial airgap flux density spectra between the investigated machines.

torque for the proposed Vernier machine, as shown in Table 2, is almost 7%, 39% and 207% higher than Design 1, SPM-V and conventional SPM machines, respectively. The on-load torque ripples [$(T_{\max} - T_{\min})/T_{\mathrm{av}} \times 100\%$, where $T_{\max}$ and $T_{\min}$ are the maximum and the minimum values of on-load torque during one electrical period] shown in Table 2, suggest that they are mainly driven by the cogging torque (of 6th harmonic order) as shown in Figure 8b.

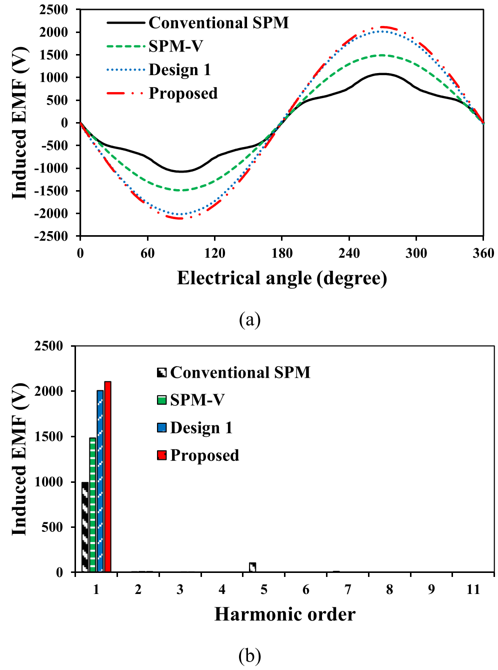

FIGURE 6 | Comparison of induced EMF between the conventional SPM and SPM-V machines. (a) Waveforms and (b) spectra.

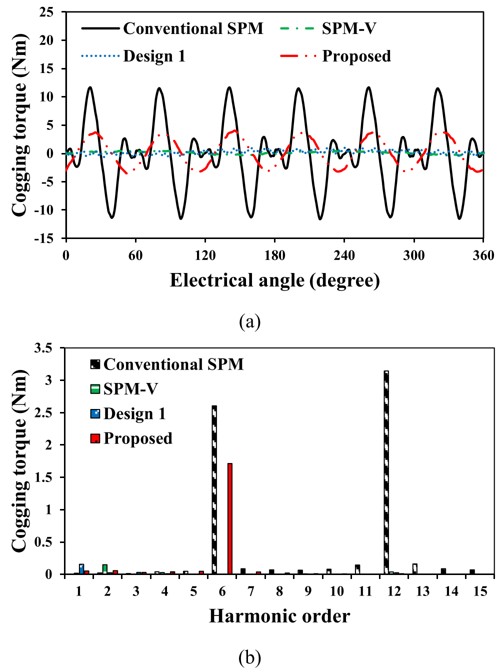

FIGURE 7 | Comparison of cogging torque between the conventional SPM and SPM-V machines. (a) Waveforms and (b) spectra.

In order to investigate the contribution of airgap flux density harmonics to the on-load torque, the Maxwell stress tensor method is adopted, and the two Vernier machines with PMs installed on both the rotor and stator, that is, Design 1 and the proposed machine were compared as shown in Figure 9. This confirms the torque-producing mechanism discussed in section 2.2. Since the proposed Vernier machine uses a larger PM volume in the rotor than Design 1, as shown in Table 2, the torque contribution from the 11th order harmonic is higher.

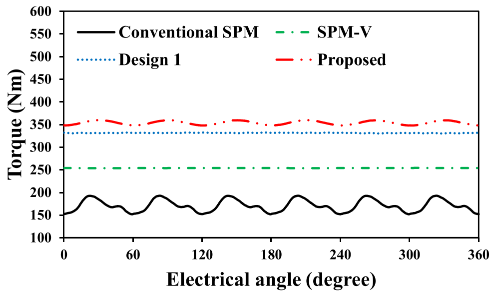

(a)

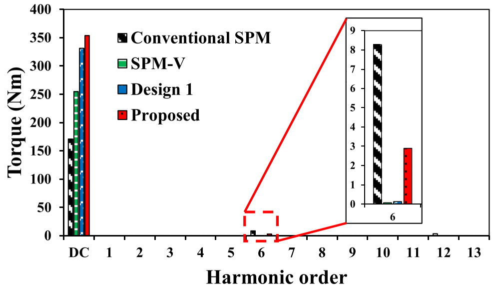

(b)

FIGURE 8 | Comparison of torques between the conventional SPM and SPM-V machines. (a) Waveforms and (b) spectra.

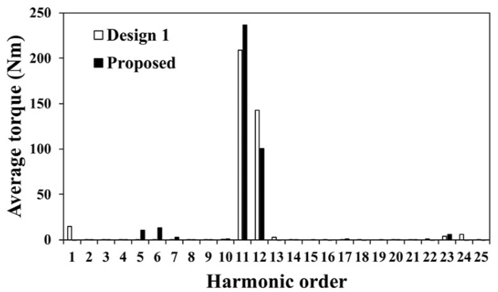

FIGURE 9 | Comparison of torque producing harmonic components in airgap flux density between Design 1 and the proposed Vernier machine.

The comparison of torque-current characteristics is shown in Figure 10. The phase current is gradually increased to around twice the rated current. The proposed Vernier machine always produces higher torque than the other investigated machines.

3.3 | Power Factor

Generally, one of the major disadvantages of the Vernier machines is that they often have a relatively low power factor compared to conventional SPM machines [29]. This would mean that for the same active power, they would need to have more expensive power converter because of larger apparent power. The comparison of power factor between the conventional SPM and Vernier machines is shown in Table 2. It is found that the conventional SPM machine has a unity power factor. However, the Vernier machines generally have a poorer power factor, which is because of their higher synchronous reactance resulting from higher inductances and operating

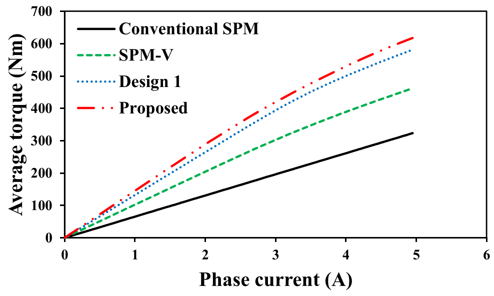

FIGURE 10 | Comparison of torque-current (rms) characteristics between the conventional SPM and Vernier machines including measured results.

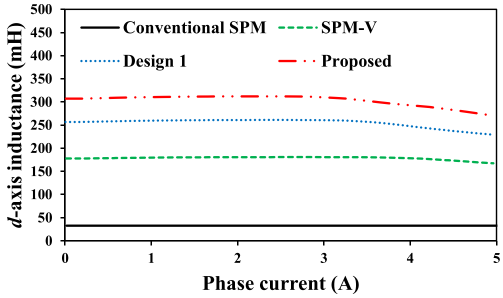

FIGURE 11 | Comparison of *d*-axis inductance (without the presence of PMs) between the conventional SPM and Vernier machines.

frequencies (see Table 2). In addition, it is also found that the proposed Vernier machine achieves a relatively lower power factor of 0.68 compared to 0.74 and 0.69 for Design 1 and the SPM-V machine, respectively. This is mainly because although the proposed Vernier machine could produce higher induced EMF than Design 1, its relatively higher winding inductance as shown in Figure 11, has resulted in a lower power factor. However, compared to the SPM-V machine, the proposed machine can achieve much higher torque with a comparable power factor.

3.4 | Torque to Cost and Torque to Mass

Compared to geared machines, the larger size of the direct-drive counterparts will result in higher costs and heavier mass. Hence it is important to evaluate the torque to cost (T2C) and torque to mass (T2M) of these investigated machines for a fairer comparison. For the calculation of cost and mass, only the active material is considered. The mass density and the cost of each active material component used for the calculation are 7650 kg/m^3 and 2.5 €/kg for silicon steel, 7400 kg/m^3 and 50 €/kg for NdFeB and 8940 kg/m^3 and 8 €/kg for copper. The comparison of the active material cost and T2C between the machines is shown in Figure 12 and Table 3. The cost of the machines is mainly driven by the PM volume. As mentioned before, the SPM-V machine uses a lower PM volume and hence a lower PM cost. The second major cost is the copper wires. Conventional SPM machine has a relatively lower copper cost due to their shorter end-winding lengths. For the same airgap diameter and coil pitch (slot/pole) as the conventional SPM machines, the Vernier machines have a longer end-winding length because of their lower slot/pole number combinations. Compared to other machines, the proposed Vernier machine uses only half of the slots for windings. Hence for the same phase current, the stator slot depth for the proposed machine is almost doubled compared to the other machines, increasing the cost of the stator core. This increased slot depth can be visualised in Figure 4d. Although the overall cost of the proposed Vernier machine is higher, the T2C ratio is found to be 74% and 15% higher than the conventional SPM and SPM-V machines, respectively. Whereas, its only 3% lower compared to Design 1.

The comparison of the mass of the active components is shown in Figure 12b. It is observed that the stator core, the main component driving the mass, is much heavier for the proposed machine because of its large slot depths. This has increased the overall mass of this machine and therefore the T2M is much lower (by 30%) than Design 1 and SPM-V machine as shown in Figure 12b. However, the T2M is still significantly higher (by 47%) than the conventional SPM machines.

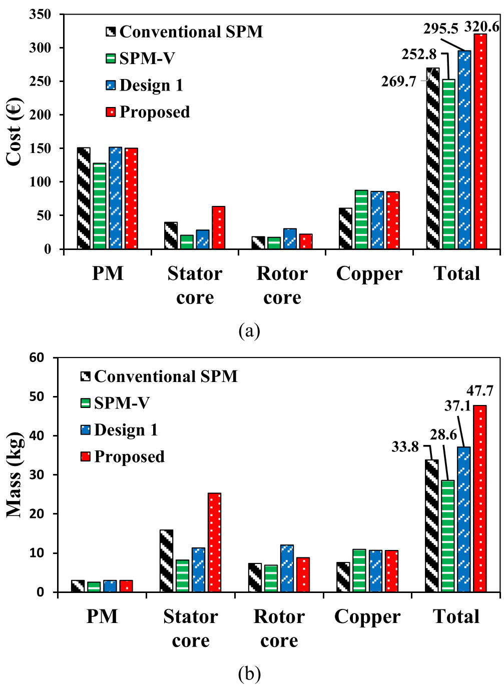

FIGURE 12 | Comparison of the active components (a) cost in Euros and (b) mass in kg.

3.5 | EM Losses and Efficiency

For calculating the efficiency, only the EM losses, that is, the PM eddy current, iron core and copper losses were considered. Unlike the conventional PM machines, the Vernier machines have high eddy current losses in the PMs [30] and rotor (solid) back iron. This is because their fundamental armature MMF rotates asynchronously with the rotor. Hence, the rotor back irons of all the machines investigated in this paper are laminated which is similar to the stator core. However, a laminated rotor may be a challenge for large multi-MW direct-drive offshore wind applications. Hence, Vernier machines may require a solid frame to support the laminated rotor core. The prototype built and tested for the proposed Vernier machine incorporates these design requirements and is discussed in section 4. To reduce the PM eddy current loss in the Vernier machines, 2 circumferential segmentations were used for all the radially magnetised PMs. No segmentations have been used for the stator Halbach PMs of Design 1. Similarly, no segmentation has been used for the conventional SPM machines as their PM eddy current loss is negligible. The comparison of EM losses between the conventional SPM and Vernier machines is shown in Figure 13.

It can be observed that Vernier machines have relatively higher losses compared to the conventional SPM machines. This is because of their higher operating frequencies resulting in higher iron core losses. Also, the longer end-windings result in higher copper loss. Although the proposed Vernier machine has higher losses, its relatively high torque helps achieve an overall efficiency of 96.18% which is better than the conventional SPM (95.1%) and SPM-V (95.48%) machines. However, Design 1 with high torque and relatively lower losses has the maximum efficiency (96.36%) marginally better than the proposed Vernier machine.

3.6 | Thermal Performance

Two simplified 3D models were constructed using JMAG software package for both Design 1 and the proposed machine to evaluate their thermal performances. To obtain essential parameters such as the convection coefficient of the rotor's outer surface and the thermal resistance of the air gap, two corresponding models of typical outer rotor SPM machines were built in motor-CAD. Unlike the proposed machines, these typical SPM machines do not have magnets on the stator; instead, these

TABLE 3 | Performance comparison.

Parameter	SPM-V machine	Design 1 [1]	Proposed machine	With through-slots
Induced EMF (V)	857	1160	1216.5	1208.5
Average torque (Nm)	254	331	354	352
Cogging torque (%)	0.36	0.5	2.1	2.1
Torque ripple (%)	0.38	0.63	3.4	3.3
Power factor	0.69	0.74	0.68	0.675
T2M (Nm/kg)	1.76	1.77	1.46	1.67
T2C (Nm/€)	1.59	1.77	1.74	1.82
Efficiency (%)	95.5	96.36	96.18	96

areas are replaced by iron. However, these machines are assumed to have the same convection coefficient and air gap thermal resistance. The rotor's outer surface dissipates heat through forced air convection because of rotation and radiation. In motor-CAD, the obtained heat transfer coefficient for forced air convection is 6.8 W/m^2/°C, and for radiation, it is 6.3 W/m^2/°C. Consequently, in the JMAG thermal model, the rotor's outer surface is assigned a combined heat transfer coefficient of 13.1 W/m^2/°C with an ambient temperature of 25°C. The inner surface of the stator is considered to be cooled down by natural convection. In motor-CAD, the obtained heat transfer coefficient for natural air convection is 3.9 W/m^2/°C and for radiation, it is 6.3 W/m^2/°C. Consequently, in the JMAG thermal model, the stator's inner surface is assigned a combined heat transfer coefficient of 10.2 W/m^2/°C with an ambient temperature of 25°C. Other essential thermal parameters are listed in Table 4 with the various losses shown in Figure 13. The winding part is represented using equivalent thermal conductivity in different directions obtained from motor-CAD software. The copper filling factor of the slot is 0.4, with corresponding thermal conductivities of 0.59 W/m·K in the radial and tangential directions, and 251 W/m·K in the axial direction. An equivalent air gap with a thickness of 0.037 mm introduces the contact thermal resistance between the housing and rotor iron. It is also worth noting that in JMAG, the airgap region is modelled using two identical thermal resistances (1.45°C/W) because of convection—one linked to the rotor surface and the other to the stator surface—connected in series to establish a heat flow path between the stator and rotor. As a result, the JMAG model integrates both finite element analysis and a lumped parameter network with the latter specifically applied to the airgap region.

The temperature distribution of the investigated machines at 170 rpm is shown in Figure 14. For clarity, only the temperature on the stator is presented since the magnets, being adjacent to the windings, exhibit the highest temperature. It can be observed that Design 1 has a lower overall temperature, primarily because of the lower stator core iron loss (see Figure 13). However, the temperature gradients between the slots and magnets are around 2°C–3°C for both Design 1 and the proposed machine, indicating that the location of the magnets does not significantly impact PM thermal performance of these two machines.

3.7 | PM Demagnetisation

The demagnetisation analysis is performed under a symmetrical 3-phase short circuit. It is to be noted that the Halbach arrays in

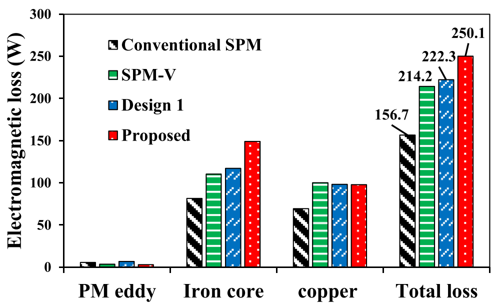

FIGURE 13 | Comparison of EM losses between conventional SPM and Vernier machines.

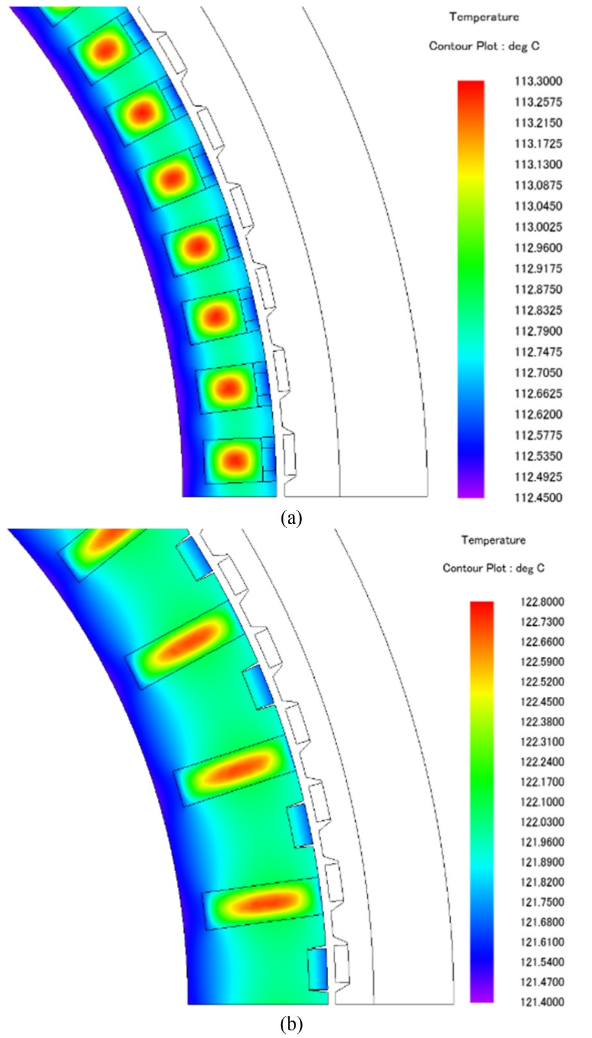

FIGURE 14 | Temperature distributions of (a) Design 1 and (b) proposed design.

TABLE 4 | Thermal parameters of different machine materials.

	Thermal conductivity (W/m/°C)	Specific heat (J/kg/°C)	Density (kg/m^3)
Housing	168	833	2790
Iron	30	460	7650
Coil	0.59 (radial) & 251(axial)	385	8933
Magnet	7.6	460	7500
Air (25°C)	0.026	1004	1.185

Design 1 are close to the windings and hence may experience higher temperatures than the stator PMs in the proposed Vernier machine. However, for simplification, the operating temperature of both the rotor and stator PMs is assumed to be 60°C which gives a knee point of 0.12T, a *Br* of 1.152T and a *Hc* of −871kA/m. The comparison of the *d*-axis short circuit current and *d*-axis flux linkage (at peak *d*-axis current [$I_{d,\text{peak}}$]) is shown in Figure 15. Because of the relatively high inductance of the Vernier machines (see Figure 11), the $I_{d,\text{peak}}$ is almost 7 times lower than that of the conventional SPM machines as shown in Figure 15a. Since the Vernier machines are harmonically coupled, the rotational direction of the rotor is opposite to that of the conventional SPM machines and hence the polarity of *d*-axis currents is opposite. The $I_{d,\text{peak}}$ is found to be almost the same for all the Vernier machines. The *d*-axis flux linkage of the Vernier machines is therefore proportional to their inductances, that is, the proposed machine has the highest *d*-axis flux linkage followed by Design 1 as shown Figure 15b.

The flux distribution in the machine and the flux density distribution in the PMs at the instant of $I_{d,\text{peak}}$ is compared between Design 1 and the proposed Vernier machine as shown in Figure 16. The coloured region (< 0.12T) indicates the demagnetised area in the PM. It can be observed that both the rotor and stator PMs are partially demagnetised in Design 1. However, in the proposed Vernier machine, even with a higher *d*-axis flux linkage, the PMs are not demagnetised. This is because, for the same PM volume between the two machines, the proposed machine can have thicker PMs as only half of the stator slots are installed with PMs. A thicker PM improves the irreversible demagnetisation withstand capability. For the same reasons, both the conventional SPM and SPM-V machines did not show any demagnetisation in the PMs. It is worth noting that, if a higher temperature of the PMs next to windings is considered (very much possible as stator windings generally have a high operating temperature), the demagnetisation withstand capability of Design 1 may be further worsened.

The above results show that the proposed Vernier machine has a comparable torque, power factor, T2C, efficiency and a better demagnetisation performance compared to the existing Design 1. Moreover, they show superior performance compared to the conventional SPM and SPM-V machines. However, one of the drawbacks of the proposed Vernier machine is their bigger stator core increasing their mass and thereby lowering the T2M ratio. To improve their T2M ratio, through-slots are proposed below the stator PMs and are discussed in detail in the next section.

3.8 | Proposed Vernier Machine With Through-Slots

The comparison of the 2D one pole pair model of the proposed Vernier machine with and without through-slots is shown in Figure 17.

The dimensions of the through-slots are optimised to maximise the T2M ratio. The performance comparison of the proposed Vernier machines with and without through-slots is shown in Table 3. It can be observed that the T2M ratio is improved by 14% (from 1.46 to 1.67) compromising only 0.7% and 0.18% of the average torques and efficiencies, respectively. Through-slots also help improve the T2C ratio by 4.6% making it better than Design 1. Apart from using these through-slots for reducing the mass of the machine, they can also be used as ventilation ducts

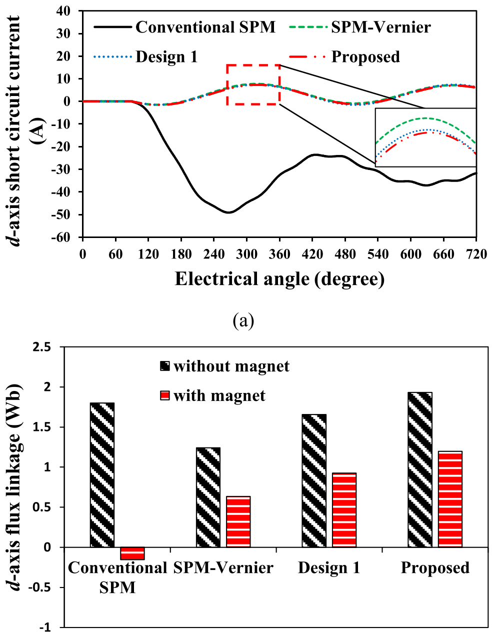

(a)

(b)

FIGURE 15 | Comparison of *d*-axis short-circuit current and flux linkage between the conventional SPM machine and Vernier machines. (a) *d*-axis current under 3-phase short-circuit and (b) *d*-axis flux linkage at peak *d*-axis current ($I_{d,\text{peak}}$) with and without PMs excited.

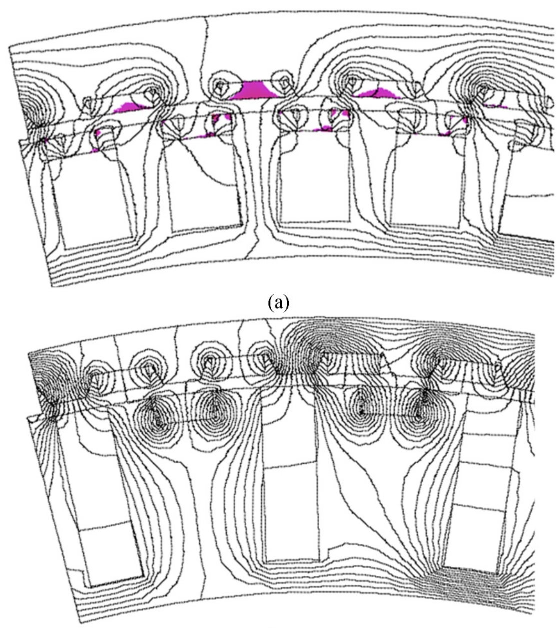

(a)

(b)

FIGURE 16 | Comparison of *d*-axis flux distribution in the machine and flux density distribution in the PMs at the instant of $I_{d,\text{peak}}$. (a) Design 1 and (b) proposed Vernier machine. The coloured region indicates the demagnetised areas in the PMs.

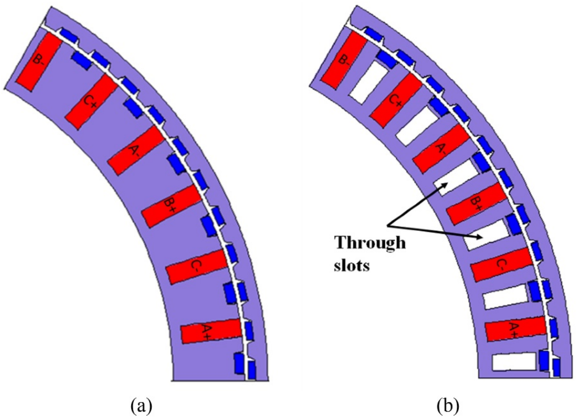

FIGURE 17 | Comparison of one pole pair model of the proposed Vernier machine. (a) Without through-slots and (b) with through-slots.

to improve the cooling. Large direct-drive wind generators will have multiple axial stator core packages. Therefore, the forced/natural air through the airgap of the machine can circulate along these through-slots to improve the thermal performance of the machine. As these through-slots are near the stator PMs and windings, they can be effective in removing the heat because of copper and PM eddy losses.

4 | Experimental Validation

To validate the simulations, a prototype of the proposed Vernier machine was constructed, and the stator and rotor laminates as well as the completed stator and rotor are shown in Figure 18a–c. The machine specifications for this prototype match those listed in Table 2. The prototype, mounted on the test rig, is illustrated in Figure 18d.

4.1 | Noload Tests

To measure the phase EMF, the protype machine was spun at its rated speed by the drive motor shown in Figure 18d. Three-phase EMFs were measured, and the measured phase A EMF has been used as an example to compare against the simulated result as shown in Figure 19. Since the proposed machine generates predominantly sinusoidal EMF with minimal harmonic components, the spectra are not presented here because of space limitations.

Overall, there is a generally good agreement between the simulated and measured results, albeit with a slight discrepancy where the measured EMF is marginally lower than the simulated counterpart. It is worth noting that because of the external rotor structure, the prototype machine has only one bearing on the left-hand side end-plate as shown in Figure 18d. This single bearing arrangement posed challenges in maintaining perfect concentricity between the stator and rotor, resulting in unavoidable eccentricity during testing. The impact of rotor eccentricity on machine performance will be discussed in the following section.

The Vernier machine exhibits a phase resistance around 5Ω. The relatively high phase resistance is mainly because of the

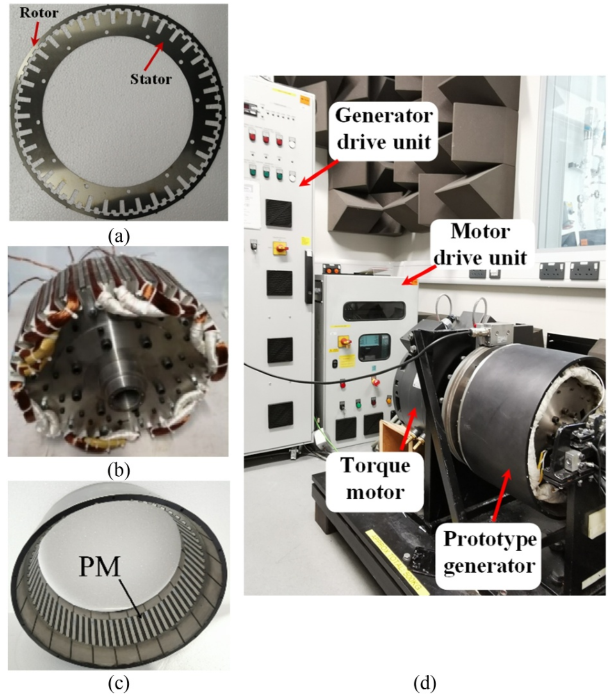

FIGURE 18 | Proposed Vernier generator prototype. (a) Stator and rotor laminates, (b) stator, (c) rotor and (d) complete machine on test rig.

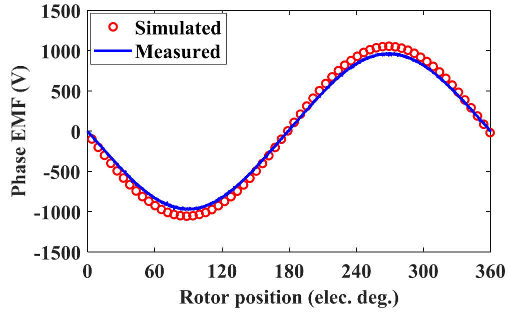

FIGURE 19 | Simulated and measured phase back-EMF.

large number of turns per phase (832) as shown in Table 2. The measured *d*-axis inductance is approximately 357 mH which is slightly higher than the simulated value of around 310 mH shown in Figure 11. This discrepancy is primarily attributed to the end-windings that were not accounted for in the 2D FE models used for calculating the *d*-axis inductance.

4.2 | Eccentricity Analysis

To assess the impact of rotor eccentricity on machine performance, the phase EMF and rated torque were calculated for various levels of eccentricity, ranging from 0 mm (no eccentricity) to 0.6 mm. It is worth noting that only static eccentricity is considered, and it occurs in *x*-axis. The finite element results are shown in Figure 20. As rotor eccentricity causes a non-uniform airgap, it was observed that both the phase EMF and on-load torque generally increased. However, this also led to a rise in the peak-to-peak variation of the on-load torque.

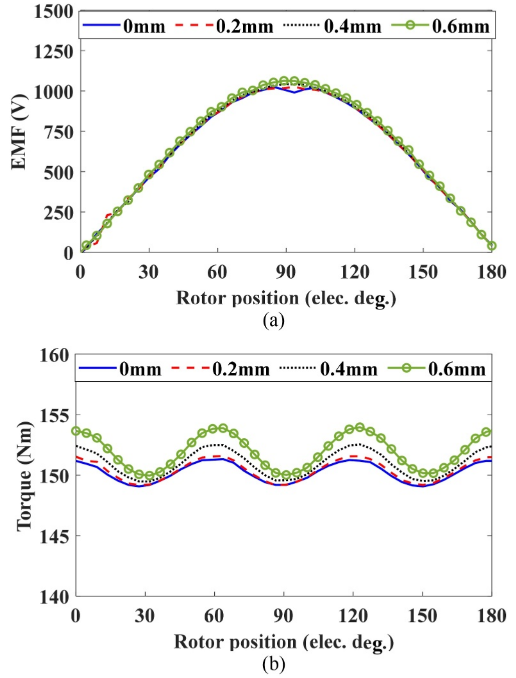

FIGURE 20 | (a) EMF and (b) rated torque versus rotor eccentricity.

Despite best effort being made to mitigate the rotor eccentricity, it might have contributed to the observed discrepancy between the simulated and measured phase EMFs (see Figure 19). It is also worth noting that the cogging torque of the proposed Vernier machine is very small, which cannot be accurately measured using the existing test rig shown in Figure 18d.

4.3 | Onload Tests

The prototype machine was tested as a generator with its speed and torque varied to simulate different operating conditions. It is important to note that this operating mode differs from the simulations, where the proposed machine was operated as a motor. This approach was chosen for practical reasons, as the test rig and associated control algorithms were designed to operate the prototype machine as a generator. However, this difference should not affect the accuracy of the investigation. The distinction between motoring and generating modes lies only in the current phase angle (not its magnitude) which determines the sign of the output torque but does not affect its magnitude.

The onload torque against rotor position and average torque against phase rms current were measured, and compared against the simulated results as shown in Figure 21. Again, as for the phase EMFs, the measured average torque is also slightly different from the simulated one, primarily attributed to the aforementioned rotor eccentricity.

5 | Conclusion

This paper proposes a Vernier machine with an improved stator design, incorporating dedicated stator slots for the installation of stator permanent magnets (PMs). The machine features PMs on

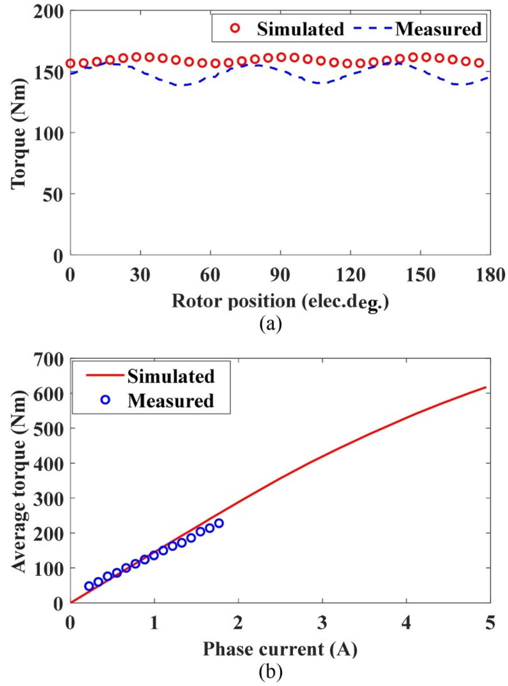

FIGURE 21 | Comparison between simulated and measured results. (a) On-load torque waveform at an rms current of around 1A, and (b) average torque versus phase rms current.

both the rotor and stator as well as form-wound coils, specifically optimised for direct-drive wind power applications. This innovation addresses the magnet installation challenges of the existing Vernier topology, where stator PMs and windings share the same slots (Design 1). The electromagnetic performance of the proposed Vernier machine is compared with conventional surface-mounted permanent magnet (SPM) machines, SPM Vernier (SPM-V) machines and Design 1. The study reveals that the proposed Vernier machine uses both odd and even harmonics to generate torque, and it can outperform the conventional SPM and SPM-V machines. Although it shows marginally lower or comparable electromagnetic performance to Design 1, its other benefits such as enhanced demagnetisation withstand capability and easier installation of stator radial PMs, make the proposed Vernier machine a promising candidate for large direct-drive wind power applications. Furthermore, the introduction of through-slots beneath the stator PMs can further enhance performance metrics such as torque-to-cost and torque-to-mass ratios. The numerical results have been validated through tests on a prototype.

Author Contributions

Dileep Kumar Kana Padinharu: writing – original draft. **Guang-Jin Li:** writing – review and editing. **Guan-Bo Zhang:** formal analysis. **Zi-Qiang Zhu:** writing – review and editing. **Peng Wang:** validation. **Richard Clark:** writing – review and editing. **Ziad Azar:** Writing – review and editing.

Acknowledgements

This work is supported by the UK EPSRC Prosperity Partnership 'A New Partnership in Offshore Wind' under Grant No. EP/R004900/1. For the purpose of open access, the author has applied a Creative Commons

Attribution (CC BY) licence to any Author Accepted Manuscript version arising.

Conflicts of Interest

The authors declare no conflicts of interest.

Data Availability Statement

Data subject to third party restrictions.

References

1. K. Xie, D. Li, R. Qu, and Y. Gao, "A Novel Permanent Magnet Vernier Machine With Halbach Array Magnets in Stator Slot Opening," *IEEE Transactions on Magnetics* 53, no. 6 (2017): 1–5, https://doi.org/10.1109/tmag.2017.2658634.

2. G. van de Kaa, M. van Ek, L. M. Kamp, and J. Rezaei, "Wind Turbine Technology Battles: Gearbox Versus Direct Drive - Opening up the Black Box of Technology Characteristics," *Technological Forecasting and Social Change* 153 (2020): 119933, https://doi.org/10.1016/j.techfore.2020.119933.

3. A. Rehman and B. Kim, "Design and Analysis of 15 MW SPM Vernier Generator for Direct-Drive Wind Turbine Applications," *Energies* 16, no. 3 (2023): 1–14, https://doi.org/10.3390/en16031094.

4. L. Cao, Y. Zuo, X. Zhu, S. Xie, and C. H. T. Lee, "Investigation of Permanent-Magnet Vernier Machine With Fractional-Slot Nonoverlapping Windings for Direct-Drive Application," *IEEE Transactions on Transportation Electrification* 10, no. 2 (2024): 3383–3395, https://doi.org/10.1109/tte.2023.3302285.

5. Y. Yu, F. Chai, Y. Pei, M. Doppelbauer, and C. H. T. Lee, "Investigation of Power Factor Characteristic in Permanent Magnet Motors for In-Wheel Direct Drive Application," *IEEE Transactions on Energy Conversion* 39, no. 3 (2024): 1699–1710, https://doi.org/10.1109/tec.2024.3360048.

6. K. Xie, D. Li, R. Qu, X. Ren, M. R. Shah, and Y. Pan, "A New Perspective on the PM Vernier Machine Mechanism," *IEEE Transactions on Industry Applications* 55, no. 2 (2019): 1420–1429, https://doi.org/10.1109/tia.2018.2880144.

7. D. K. K. Padinharu, G. J. Li, Z. Q. Zhu, et al., "Scaling Effect on Electromagnetic Performance of Surface-Mounted Permanent-Magnet Vernier Machine," *IEEE Transactions on Magnetics* 56, no. 5 (2020): 1–15, https://doi.org/10.1109/tmag.2020.2980500.

8. L. Xu, G. Liu, W. Zhao, J. Ji, and X. Fan, "High-Performance Fault Tolerant Halbach Permanent Magnet Vernier Machines for Safety-Critical Applications," *IEEE Transactions on Magnetics* 52, no. 7 (2016): 1–4, https://doi.org/10.1109/tmag.2016.2524541.

9. W. Liu and T. A. Lipo, "Analysis of Consequent Pole Spoke Type Vernier Permanent Magnet Machine With Alternating Flux Barrier Design," *IEEE Transactions on Industry Applications* 54, no. 6 (2018): 5918–5929, https://doi.org/10.1109/tia.2018.2856579.

10. X. Li, K. T. Chau, and M. Cheng, "Comparative Analysis and Experimental Verification of an Effective Permanent-Magnet Vernier Machine," *IEEE Transactions on Magnetics* 51, no. 7 (2015): 1–9, https://doi.org/10.1109/tmag.2014.2359853.

11. S. U. Chung, J. W. Kim, B. C. Woo, D. K. Hong, J. Y. Lee, and D. H. Koo, "A Novel Design of Modular Three-Phase Permanent Magnet Vernier Machine With Consequent Pole Rotor," *IEEE Transactions on Magnetics* 47, no. 10 (2011): 4215–4218, https://doi.org/10.1109/tmag.2011.2157324.

12. H. Zhou, W. Tao, C. Zhou, Y. Mao, G. J. Li, and G. Liu, "Consequent Pole Permanent Magnet Vernier Machine With Asymmetric Air-Gap Field Distribution," *IEEE Access* 7 (2019): 109340–109348, https://doi.org/10.1109/access.2019.2933657.

13. D. Li, R. Qu, and T. A. Lipo, "High-Power-Factor Vernier Permanent-Magnet Machines," *IEEE Transactions on Industry Applications* 50, no. 6 (2014): 3664–3674, https://doi.org/10.1109/tia.2014.2315443.

14. A. Allahyari and H. Torkaman, "A Novel High-Performance Consequent Pole Dual Rotor Permanent Magnet Vernier Machine," *IEEE Transactions on Energy Conversion* 35, no. 3 (2020): 1238–1246, https://doi.org/10.1109/tec.2020.2980146.

15. T. Zou, D. Li, R. Qu, D. Jiang, and J. Li, "Advanced High Torque Density PM Vernier Machine With Multiple Working Harmonics," *IEEE Transactions on Industry Applications* 53, no. 6 (2017): 5295–5304, https://doi.org/10.1109/tia.2017.2724505.

16. H. Li, Z. Q. Zhu, and Y. Liu, "Optimal Number of Flux Modulation Pole in Vernier Permanent Magnet Synchronous Machines," *IEEE Transactions on Industry Applications* 55, no. 6 (2019): 5747–5757, https://doi.org/10.1109/tia.2019.2930026.

17. G. Yang, J. Li, and M. Lin, "Design and Analysis of Novel Modular Stator Axial-Flux Permanent Magnet Vernier Machine With Improved Power Factor," *IEEE Access* 11 (2023): 108580–108590, https://doi.org/10.1109/access.2023.3319047.

18. Y. Zhao, X. Ren, X. Fan, D. Li, and R. Qu, "A High Power Factor Permanent Magnet Vernier Machine With Modular Stator and Yokeless Rotor," *IEEE Transactions on Industrial Electronics* 70, no. 7 (2023): 7141–7152, https://doi.org/10.1109/tie.2022.3199863.

19. Y. Zheng, W. Xiang, M. Kang, L. Wu, and Y. Fang, "Analysis of Dual PM Vernier Machines With Different Consequent-Pole Pm Topologies," *IEEE Transactions on Industry Applications* 59, no. 2 (2023): 1670–1677, https://doi.org/10.1109/tia.2022.3228225.

20. H. Chen, Z. Zhu, Z. Zhang, and H. Wang, "Comparative Analysis of Consequent-Pole PM Vernier Machines With Different Rotor Types," *IEEE Transactions on Transportation Electrification* 10, no. 1 (2024): 450–461, https://doi.org/10.1109/tte.2023.3288605.

21. D. K. Jang and J. H. Chang, "Design of a Vernier Machine With Pm on Both Sides of Rotor and Stator," *IEEE Transactions on Magnetics* 50, no. 2 (2014): 877–880, https://doi.org/10.1109/tmag.2013.2284509.

22. W. Zhao, X. Sun, J. Ji, and G. Liu, "Design and Analysis of New Vernier Permanent-Magnet Machine With Improved Torque Capability," *IEEE Transactions on Applied Superconductivity* 26, no. 4 (2016): 1–5, https://doi.org/10.1109/tasc.2016.2518927.

23. G. Xu, G. Liu, M. Chen, X. Du, and M. Xu, "Cost-Effective Vernier Permanent-Magnet Machine With High Torque Performance," *IEEE Transactions on Magnetics* 53, no. 11 (2017): 1–4, https://doi.org/10.1109/intmag.2017.8007746.

24. J. Huang, W. Fu, S. Niu, and X. Zhao, "Comparative Analysis of Different Permanent Magnet Arrangements in a Novel Flux Modulated Electric Machine," *IEEE Access* 9 (2021): 14437–14445, https://doi.org/10.1109/access.2021.3052545.

25. G. Xu, L. Jian, W. Gong, and W. Zhao, "Quantitative Comparison of Flux-Modulated Interior Permanent Magnet Machines With Distributed Windings and Concentrated Windings," *Progress in Electromagnetics Research* 129 (2012): 109+–123, https://doi.org/10.2528/pier12040901.

26. D. K. Kana Padinharu, G.-J. Li, Z.-Q. Zhu, P. Wang, R. Clark, and Z. Azar, "Comparison of Direct-Drive Vernier Wind Generators for Potential Use at ≥ 10 MW Power Level," *IET Electric Power Applications* n/a, no. n/a (2024): 1–14, https://doi.org/10.1049/elp2.12477.

27. S. Hyoseok, N. Niguchi, and K. Hirata, "Characteristic Analysis of Surface Permanent-Magnet Vernier Motor According to Pole Ratio and Winding Pole Number," *IEEE Transactions on Magnetics* 53, no. 11 (2017): 1–4, https://doi.org/10.1109/tmag.2017.2702278.

28. A. Toba and T. A. Lipo, "Generic Torque-Maximizing Design Methodology of Surface Permanent-Magnet Vernier Machine," *IEEE Transactions on Industry Applications* 36, no. 6 (2000): 1539–1546, https://doi.org/10.1109/28.887204.

29. Z. S. Du and T. A. Lipo, “Torque Performance Comparison Between a Ferrite Magnet Vernier Motor and an Industrial Interior Permanent Magnet Machine,” *IEEE Transactions on Industry Applications* 53, no. 3 (2017): 2088–2097, https://doi.org/10.1109/tia.2017.2673812.

30. D. K. K. Padinharu, G. J. Li, Z. Q. Zhu, R. Clark, A. Thomas, and Z. Azar, “AC Losses in Form-Wound Coils of Surface Mounted Permanent Magnet Vernier Machines,” *IEEE Transactions on Magnetics* 58, no. 6 (April 2022): 1–15, https://doi.org/10.1109/tmag.2022.3170658.